---

**Article:**
Dede, A.J.O. orcid.org/0000-0002-3619-4631, Mishra, A., Marzban, N. et al. (3 more authors) (2022) Intra- and inter-regional dynamics in cortical-striatal-tegmental networks. Journal of Neurophysiology, 128 (1). pp. 1-18. ISSN: 0022-3077

https://doi.org/10.1152/jn.00104.2022

---

american physiological society

JNP JOURNAL OF NEUROPHYSIOLOGY

*J Neurophysiol* 128: 1–18, 2022.
*First published June 1, 2022; doi:10.1152/jn.00104.2022*

RESEARCH ARTICLE

*Computational Neuroscience*

# Intra- and inter-regional dynamics in cortical-striatal-tegmental networks

**Adam J. O. Dede,[1,2,3] Ashutosh Mishra,[4,5] Nader Marzban,[4,5] Robert Reichert,[4,5] Paul M. Anderson,[4,5] and Michael X. Cohen[4,5]**

[1]*Department of Psychology, University of Sheffield, Sheffield, United Kingdom;* [2]*Department of Pharmaceutical Care, School of Pharmaceutical Sciences, University of Phayao, Phayao, Thailand;* [3]*Unit of Excellence on Clinical Outcomes Research and Integration (Unicorn), School of Pharmaceutical Sciences, University of Phayao, Phayao, Thailand;* [4]*Radboud University Medical Center, Radboud University Nijmegen, Nijmegen, The Netherlands; and* [5]*Donders Institute for Brain, Cognition and Behaviour and Faculty of Social Sciences, Radboud University, Nijmegen, The Netherlands*

## Abstract

It is increasingly recognized that networks of brain areas work together to accomplish computational goals. However, functional connectivity networks are not often compared between different behavioral states and across different frequencies of electrical oscillatory signals. In addition, connectivity is always defined as the strength of signal relatedness between two atlas-based anatomical locations. Here, we performed an exploratory analysis using data collected from high-density arrays in the prefrontal cortex (PFC), striatum (STR), and ventral tegmental area (VTA) of male rats. These areas have all been implicated in a wide range of different tasks and computations including various types of memory as well as reward valuation, habit formation and execution, and skill learning. Novel intraregional clustering analyses identified patterns of spatially restricted, temporally coherent, and frequency-specific signals that were reproducible across days and were modulated by behavioral states. Multiple clusters were identified within each anatomical region, indicating a mesoscopic scale of organization. Generalized eigendecomposition (GED) was used to dimension-reduce each cluster to a single component time series. Dense intercluster connectivity was modulated by behavioral state, with connectivity becoming reduced when the animals were exposed to a novel object, compared with a baseline condition. Behavior-modulated connectivity changes were seen across the spectrum, with $\delta$, $\theta$, and $\gamma$ all being modulated. These results demonstrate the brain's ability to reorganize functionally at both the intra- and inter-regional levels during different behavioral states.

**NEW & NOTEWORTHY** We applied novel clustering techniques to discover functional subregional anatomical patches that changed with behavioral conditions but were frequency specific and stable across days. By taking into account these changes in intraregional signal generator location and extent, we were able to reveal a richer picture of inter-regional functional connectivity than would otherwise have been possible. These findings reveal that the brain's functional organization changes with state at multiple levels of scale.

*clustering; electrophysiology; network connectivity*

## INTRODUCTION

Coordinated activity between brain regions is widely believed to allow neural circuits to bind cell assemblies flexibly and to orchestrate information transfer efficiently (1–3). Anatomical connections between regions constrain and predict the range of available network states that can be achieved (4–6). In addition, there can be different patterns of connectivity between areas at different oscillatory frequencies (4, 7–9).

Brain networks are often studied during a resting state (5–8, 10). Particularly during rest and in relatively long epochs of data, it has been shown that anatomical connectivity predicts functional networks well (5, 6, 9). Considering these observations, an implicit assumption is that long periods of resting state data collected from the same individual at

Correspondence: A.J.O. Dede (adam.osman.dede@gmail.com).
Submitted 18 March 2022 / Revised 25 May 2022 / Accepted 25 May 2022

different times should be largely the same because these data sets would be based on the same underlying anatomy.

An important decision in the analysis of brain network states is deciding how granularly to chunk the anatomical space of the brain. What is the size of a functional signal generator? How are these signal generators distributed? Often, the analysis depends on atlas-based anatomical parcellations. First, some measure of pairwise connectivity is calculated for all pairs of data channels, and then connectivity is averaged for all channel pairs that span two atlas-based anatomical areas. In this way, the network connectivity graph is built up one edge at a time (5, 9, 11, 12). In this type of analysis, parcellation is static even when multiple behavioral conditions are compared or the goal is to assess dynamic connectivity changes (13). An implicit assumption is that while the connections between areas may change, the anatomical extent of an area is invariant to task or behavioral state.

Here, we performed an exploratory analysis of large-scale electrophysiological data that were collected from the prefrontal cortex (PFC), striatum (STR), and ventral tegmental area (VTA) of male rats during a series of four behavioral conditions lasting several minutes each.

We developed a data-driven analysis approach to identify spatially distributed and frequency-specific clusters. These clusters were highly reproducible within animals across different recording sessions. Next, we used amplitude envelope correlations to assess between-node connectivity (14).

Our analysis revealed that when comparing data collected during two open field periods, connectivity in the delta band was reduced in the later period relative to the first, but the aggregate strength of network connectivity across frequencies did not change. Between the two open field periods, the rats were exposed to a novel object. We also found considerable changes in the anatomical extent of intraregional areas between different conditions, implying that important connections may be missed when signals are grouped statically by anatomical region. The strongest of these changes was reorganization of the functional cluster structure detected in δ band signals in the VTA. Finally, incidental interaction with a novel and later a repeated object caused a dramatic drop in network connectivity, suggesting that even small perturbations in environmental context can lead to dramatic changes in brain network state.

## METHODS

Analysis was primarily carried out using custom written MATLAB code. ANOVA tests and some figure generation was carried out in R.

### Experimental Design

The experimental procedures have been described previously (15). Briefly, all experimental procedures were performed in accordance with the EU directive on animal experimentation (2010/63/EU), and the Dutch nationally approved ethics project 2015-0129. All recordings were performed in the laboratory of M.X.C. We included five male Long–Evans TH:Cre rats (~3 mo old, weight: 350–450 g at time of recordings). Nonoverlapping findings from this data set have been reported elsewhere (15).

Electrophysiological recordings were collected from the PFC, STR, and VTA. There were 64 contacts per region. For target recording locations see Fig. 2*A*. Sixty-four electrodes covered an area of 1 × 2 mm with typical spacing of 225 μm in each shank and 330 μm between shanks in PFC. STR electrodes also covered an area of 1 × 2 mm with the same shank distance (330 μm). However, two shanks contained only tetrodes and two shanks had only single sites with typical spacing of 130 μm between single sites and 660 μm between tetrodes. VTA implants contained eight shanks of eight electrodes each and covered an area of 1.5 × 0.14 mm.

After 1 wk of training and handling habituation, each experimental session consisted of four conditions. Habituation and experimental sessions both utilized the same black plastic square box (60 × 40 × 40 cm) with bedding covering the floor. All sessions took place under well-lit conditions. First, animals were placed in an open field. Second, a novel object (e.g., a cup or toy) was presented in the middle of the box. Third, the animal was alone in the open field again. Fourth, the same object presented in the second condition was presented again. Each condition lasted between 5 and 6 min. We termed these conditions open field, novel object, open field 2, and repeat object. Rats moved freely throughout the experimental sessions. There was no delay between conditions. A camera was placed above the box to track movement (Fig. 1, *A*–*C*). A maximum of one session per animal was recorded on a single day. There were 28 recording sessions in total with each animal contributing between four and eight sessions. The difference in the number of sessions per animal was due to their participation in multiple experiments with the collection of these open field and novel object data being of secondary priority.

Using data from video recordings and DeepLabCut (16), we created binary vectors indicating interaction with the object (during encoding and retrieval conditions) and movement. These were upsampled to 1,000 Hz and aligned to LFP data.

### Statistical Analyses

The overall analysis pipeline is sketched out in Table 1.

#### *Calculating memory strength.*

For each session, the percentage of time spent interacting with the object was calculated for the novel object and repeat object periods. The percentage during repeat was subtracted from the percentage during novel. Positive values indicate that the rat spent more time exploring the object when it was novel (Fig. 1*E*).

#### *Local field potential data cleaning.*

Data were notch-filtered to remove 50 Hz line noise, ICA filtering was done, and components that appeared to capture muscle and line noise were removed, channels that appeared to be contaminated with noise by visual inspection were removed. Finally, cross-channel covariance matrices were calculated in 2,000-ms windows in steps of 100 ms. A mean covariance matrix was calculated. Epochs whose covariance matrices were more than 2 standard deviations from the mean were discarded from further analysis. Distance between epoch and mean covariance matrices was measured using matrix Euclidean distance. Covariance based cleaning

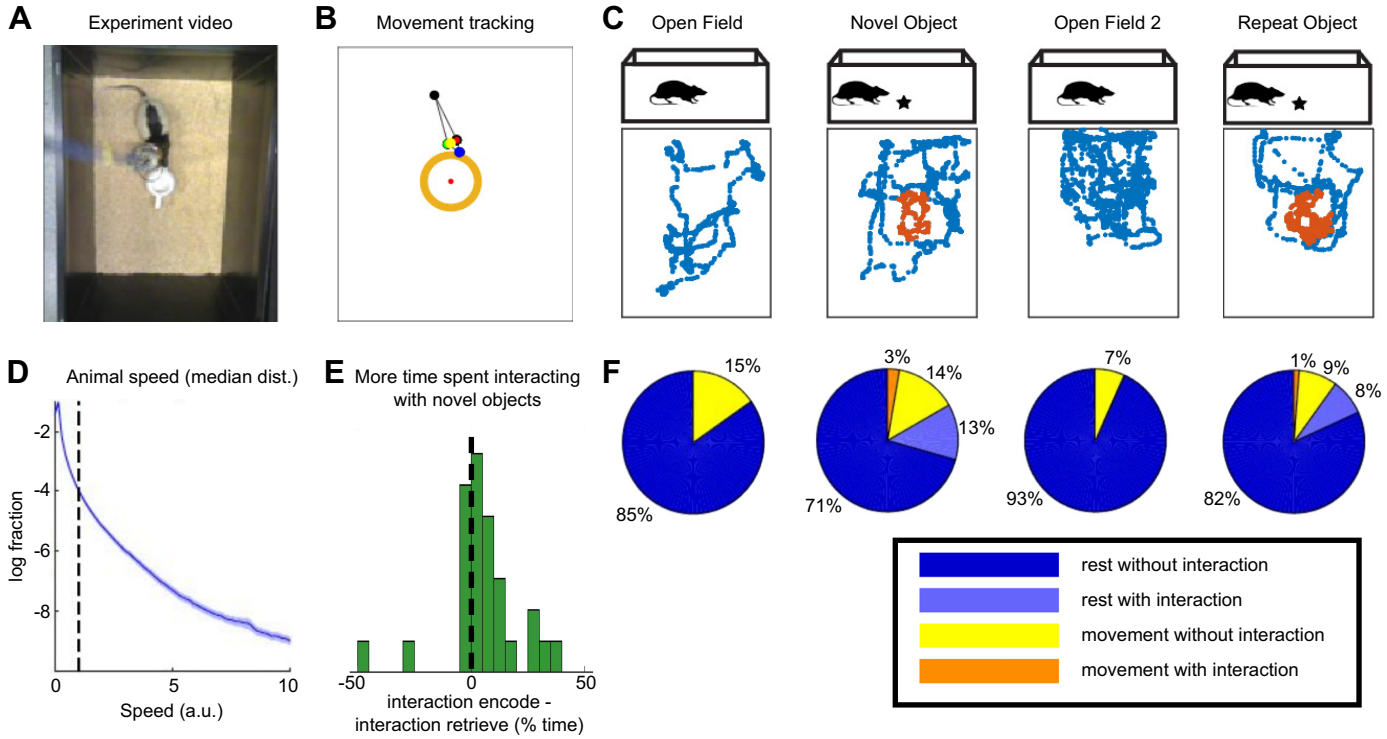


**Figure 1.** Behavioral paradigm and behavior results. *A*: still image taken from the video recording of an experimental session. The rat is exploring a white object. *B*: output of movement tracking results for the frame shown in *A*. *C*: example experimental session behavioral data. Stars indicate the presence of an object to explore (novel object and repeat object periods). During open field and open field 2 periods, there were no objects in the box. Different objects were used on different testing days. Within day, the same object was used in the novel object and repeat object periods. In the bottom of each panel is the path followed by the rat during the corresponding condition. Orange vs. blue points differentiate locations with and without interaction with the object, respectively. *D*: median distribution of animal speed movement from all the recordings. The dashed line shows the motion speed threshold separating resting from movement. *E*: histogram depicts memory for the object in terms of the percentage of time spent interacting with the object during the novel object period minus the corresponding percentage during the repeat object period. In general, more time was spent interacting with the object when it was novel [after removal of outliers more than 2 SDs below mean $t(25)=4$; $P \ll 0.001$]. *F*: pie charts show percentages of time spent in different behavioral states during each of the behavioral conditions.

was implemented using the custom covMatCleaning function (see CODE AVAILABILITY).

### *Identifying intraregional clusters.*

Data were filtered using 42 logarithmically spaced central frequencies between 2 and 150 Hz using the custom filterFGx function. After filtering, data from novel and repeat object periods were limited to periods of interaction with the object. These data included both stationary and movement periods. This was done to maximize the amount of available data for analysis and because movement periods comprised a similar proportion of data across conditions. However, results were highly similar when the main analyses were repeated on the stationary data alone (see Supplemental Data available on Github; https://github.com/adede1988/subNetworkDynamics). Channel × channel correlation matrices were calculated in nonoverlapping 2.5-s epochs. These epochs were averaged together to create a single channel × channel correlation matrix (Fig. 3*A*). In addition, the average correlation matrix was calculated 20 additional times with an evenly spaced sliding window such that a continuous 10% segment of the data was left out from each average. Effectively, this corresponded to between a half and a whole session being left out from each fold. These 20 partial averages were used for validation. This was done for each behavioral condition independently.

**Table 1.** *General analysis pipeline*

| Step | Analysis Description | Analysis Purpose |
|---|---|---|
| 1 | Granular narrowband filtering of data from each condition | Extracting key values |
| 2 | Create channel × channel correlation matrices using frequency and condition specific data | Extracting key values |
| 3 | Group channels into clusters using DBscan (Fig. 3) | Extracting key values |
| 4 | 20-fold validation, comparison to random clusters, and calculation of silhouette values (Figs. 3 and 4) | Validation and reliability |
| 5 | Combine clusters across wider frequency bands using normalized mutual information (NMI) as similarity metric (Fig. 5) | Dimensionality reduction |
| 6 | Compare clusters across frequency and condition using NMI (Fig. 6) | Inference and results |
| 7 | Create a single time series for each cluster using generalized eigen decomposition | Dimensionality reduction |
| 8 | Find connectivity between cluster time series using amplitude envelope correlation (Fig. 7) | Inference and results |

Clustering was done for each animal, condition, region, frequency, and validation fold independently. Clustering relied on a custom DBscanDynamicEpi function, whose general calculations are described here. Before clustering, we first took the correlation coefficient of each row of the channel × channel matrix compared to each column of the matrix (Fig. 3, *E*–*G*). The resulting matrix was the same size as the input matrix, but now values in the matrix represented how the map of connectivity associated with one channel correlated with the map of connectivity associated with another channel (17). Finally, we took the squared Euclidean distance comparing each row to each column of the new matrix (Fig. 3*H*). Squaring accentuates high similarities and forces all values to be positive, both of which facilitate clustering. This final matrix is referred to as the distance matrix.

The DBscan algorithm (18) was applied to distance matrices. The DBscan algorithm requires two input parameters: $K$ and epsilon. Epsilon is the search radius around each point. $K$ is the number of points that must be found within that radius to constitute a cluster. We chose the value of $K$ to be constant at eight for all clustering. This was done for two reasons. First, study by Ester et al. (18) noted that cluster discovery is largely invariant to the choice of $K$ within a reasonable range. Second, we tested all values of $K$ between 2 and 22 and visual inspection of resulting silhouette values of clustering schemes suggested that $K$ = 8 was reasonable (see Supplemental Fig. S3-1).

Our choice for the epsilon value was set dynamically for each run of DBscan. To do this, we calculated the 8-distance, which is the minimum epsilon value needed to reach eight points from a given point to be clustered. When all 8-distances in a data set are sorted and these values are plotted, natural divisions in the cluster structure of the data can be identified at points of sharp steepness in the 8-distance plot (Fig. 3*I*). Algorithmic identification of sharp steepness was identified using the running difference between sorted 8-distance values (Fig. 3*J*). The running difference between sorted 8-distance values approximates the first derivative of the curve, so peaks in the plot correspond to points of maximum steepness in the 8-distance values. We identified the first peak above a threshold for each clustering run. The threshold was the mean of the running difference plus 2 standard deviations. Threshold calculation excluded the maximum value and the surrounding five points on either side. The epsilon value corresponding to the detected peak was used for clustering (see vertical and horizontal lines in Fig. 3, *I* and *J*).

For each animal, condition, region, and frequency, clustering was performed on the correlation matrix calculated from the full recording and also on each of the 20 validation folds. Each cluster was examined across folds individually. For each fold, we asked what proportion of the channels in the cluster in the full data set were clustered together in the fold. We termed this value the agreement value. We further asked what proportion of the channels that were not a part of the cluster in the full data set were also given the same label as that which yielded the highest agreement value. We termed this value the outside value. The agreement value minus the outside value was termed the net agreement value, and clusters with an average net agreement value below 0.85 across folds were discarded as unstable (Fig. 3*D*).

### *Assessing cluster validity.*

In addition to 20-fold validity testing, which assessed cluster reliability across sessions, we assessed cluster validity through the use of several metrics. These were used to demonstrate validity but were not used to select clusters. Only the 20-fold validity testing contributed to cluster selection. We calculated four measures of cluster validity.

First, the silhouette value is a measure both of how well a point fits into a particular cluster and how poorly it fits into any other cluster. A good cluster organization will yield clusters that maximize the fit of all points to their respective clusters while minimizing the fits of points to other clusters (19, 20) (Fig. 3, *C* and *N*). Silhouette values were calculated using the custom written function getSil.

Second, we calculated the pairwise Pearson correlations among narrowband channel time series, and assessed whether those correlation coefficients were higher between channels within a cluster compared with those across different clusters (correlations were taken across conditions and frequencies, and the analysis was done separately per anatomical region) (Fig. 4*A*). Mean differences were evaluated using a $t$ test. In addition, the difference in correlation value between all of the within cluster minus between cluster correlations was calculated within each specific combination of animal, region, frequency, and condition (Fig. 4*B*). To facilitate interpretation of these correlation values, a set of randomly chosen clusters was generated. For each animal, these clusters included the same number of channels, in the same regions, at the same frequencies, and in the same conditions.

Third, we calculated the ratio of variance in mean power across the session between channels within clusters versus between all channels in a cluster's containing region. This was done separately for all clusters using frequency, region, condition, and animal-specific data. Assuming sampling from a normal population, variance is invariant to sample size. Thus, it would be expected that any randomly chosen set of channels within a region should have a similar variance in power as that observed for the region as a whole. This expectation would yield a cluster/region variance ratio of 1.0. By contrast, if clustering successfully identified channels with similar signals, then those signals might have similar mean power to each other. If this is true, then it would be expected that the cluster/region variance ratio would be below 1.0. This ratio was calculated for both the observed and randomly chosen clusters (see previous paragraph) and then compared using a two-sample Kolmogorov–Smirnov test (Fig. 4*E*).

Fourth, we evaluated the percent of variance explained by the first generalized eigendecomposition component of each observed cluster. It is expected that clusters with no unifying signal would have variance uniformly distributed across their eigenspectra. Considering that clusters contained an average of 18–26 channels (Fig. 4*G*), the expected percentage of variance explained by the top component should be ~4%–6% in the absence of any unifying signal across the cluster. Generalized eigen decomposition was performed using the custom function GEDclust.

### *Aggregating clusters.*

Normalized mutual information (NMI) was calculated for all pairs of cluster schemes within each region using *Eq. 3* from

Strehl and Ghosh (21). NMI was calculated using the custom function nmi. NMI yields a measure of the similarity between two cluster schemes of the same data. It is robust to differences in arbitrary labels (e.g., cyan vs. mauve in Fig. 5*D*) and to missing data (e.g., unclustered white electrodes in Fig. 5*D*). NMI ranges from 0 to 1. Values near 0 represent completely different clustering schemes where channels grouped into the same cluster in one scheme are in different clusters in another scheme. An NMI of 1 indicates an identical cluster scheme. NMI was calculated between cluster schemes from within the same condition. NMI values were averaged across conditions within each region, yielding a frequency × frequency matrix of cluster similarity for each region. Based on visual inspection of these matrices (Fig. 5, *A*–*C*), we decided to break frequency up into five bands. The breakpoints for these bands were chosen by a greedy search algorithm. The algorithm began with four breakpoints spaced evenly across logarithmic frequency space. For each breakpoint, the average NMI within all frequency bands and between all frequency bands was calculated. The between-NMI was subtracted from the within-NMI. This net NMI value was calculated for all possible positions of the current breakpoint such that it was at least three frequencies away from the two breakpoints (or ends) on either side of it. The breakpoint was moved to the position with the maximum net NMI value. This loop was repeated until no breakpoint moves were made. Although increasing the number of breakpoints from three to four markedly increased the final net NMI, only a marginal increase was found by increasing to five, confirming the use of four breakpoints to create five frequency bands.

Next, cluster schemes were aligned within each frequency band for each rat, condition, and region independently. This was done using the custom function greedyNMIalign. We used *Eq. 5* from Strehl and Ghosh (21) to calculate the average NMI (aNMI) between a candidate cluster scheme and all cluster schemes within a frequency band. The initial candidate cluster scheme was chosen by selecting the input cluster scheme that had the highest aNMI with the other cluster schemes within its frequency band. The initial candidate scheme was relabeled to meet two constraints: *i*) $\lambda_1 = 1$; *ii*) for all i =1, …, $n - 1$: $\lambda_i + 1 \leq \max_{j = 1, \ldots, i}(\lambda_j) + 1$ (21). Here, $\lambda$ represents the cluster label of the channel indicated by the subscript. Next, the algorithm looped over channels. For each channel, the aNMI of the whole scheme was calculated with the channel in question having each of the possible cluster labels available in the scheme. If the aNMI was higher for some other label than the channel had at the start of the loop, then the channel's label was changed. Looping continued until no further changes were made. This yielded a single cluster scheme across the entire frequency band (Fig. 5*E*).

### *Measuring changes in within-region functional structure.*

aNMI was used to measure cluster similarity between conditions (within frequency) and between frequencies (within conditions). This analysis reused the custom nmi function. In both ways of doing the analysis, each rat was considered independently. In the between-conditions analysis, cluster schemes from all four conditions were considered for one region and one frequency at a time. For each of these four cluster schemes (one from each behavioral condition), the aNMI was calculated with respect to the other three conditions. On this metric, values near 0 would indicate that within a particular frequency band, the functional structure of a region observed during a particular condition was dramatically different from other conditions. By contrast, values near 1 would indicate a high degree of functional stability between conditions. The values obtained from individual rats were subjected to a within-subjects ANOVA with the factors frequency band and condition. For conditions, dummy variables encoding linear contrasts were used to compare open field 1 versus open field 2, novel object versus repeat object, and periods with objects (novel and repeat object) versus periods without objects (open field 1 and 2). For frequencies, linear contrasts were used to compare delta versus others, theta versus others, low gamma versus others, and high gamma versus others.

The between frequency analysis was similar. Cluster schemes from all five frequencies were considered for one region and one condition at a time. For each of these five cluster schemes (one from each frequency band), the aNMI was calculated with respect to the other four conditions. Again, within-subjects ANOVA was used with the factors frequency band and condition. The same set of linear contrasts were used.

### *Measuring changes in between-region functional connections.*

To facilitate measuring connections between regions, we used generalized eigendecomposition (GED) to reduce the signals from electrodes within each cluster to a single time series. This was done using the custom GEDclust function. The goal of GED is to identify a component, defined as a weighted combination of the channel time series from within each cluster, that maximizes the power of narrowband activity relative to broadband activity:

$$\arg\max \frac{||\mathbf{w}^{\mathrm{T}}\mathbf{X}||^2}{||\mathbf{w}^{\mathrm{T}}\mathbf{Y}||^2},$$

where $\mathbf{X}$ is the narrowband-filtered data, $\mathbf{Y}$ is the broadband data, and $\mathbf{w}$ is the vector of channel weights. The solution to this optimization can be obtained from the GED on two covariance matrices: $\mathbf{S} = \mathbf{X}\mathbf{X}^{\mathbf{T}}$ and $\mathbf{R} = \mathbf{Y}\mathbf{Y}^{\mathbf{T}}$ (22, 23):

$$\mathbf{SW} = \mathbf{RW}\Lambda,$$

where $\mathbf{W}$ is the square matrix of eigenvectors, and $\Lambda$ is the diagonal matrix of eigenvalues. After solving the GED for each cluster, the eigenvector associated with the largest eigenvalue was used to calculate a weighted combination of the narrowband signals from the cluster resulting in a single time series for each cluster that explained the maximum amount of variance between the two covariance matrices. In our case, this corresponded to the narrowband specific signal relative to the broadband signal. The largest eigenvalue was divided by the sum of all eigenvalues to estimate the proportion of variance explained by the single time series (Fig. 4*F*).

Connectivity between cluster time series was assessed using amplitude envelope correlations (14). Time series were transformed into amplitude envelopes by taking the absolute value of the Hilbert transform. For every pair of cluster

time series within a given rat and condition, correlations were calculated in nonoverlapping 2.5-s windows. Windows with a correlation greater than 2 standard deviations from the mean were ignored. The remaining correlations were averaged together to obtain a connectivity strength for the pair of clusters. To assess the significance of these connectivity strength values, the same amplitude envelope correlation analysis was carried out again with one of the time series offset such that the last X data points in the time series were cut from the end and placed at the beginning of the series. X was a random value. This recalculation was carried out 1,000 times for each pair of connections. Connections whose original correlation was stronger than 950 or more of the comparison correlations were deemed significant.

To make inferences from the resulting significant connectivity graphs discovered to this point, we followed a general process similar to that implemented by van den Heuvel and Sporns (24). The general approach was to assess the network in a simplified group-level network connectivity form (Fig. 7, *A–K*) that aggregated data into a common shared network across animals, and then also to assess the network at the individual rat graph measures level (Fig. 7, *L–S*). Thus, the aggregated form of the network was more easily visualizable (Fig. 7, *A–K*) but the process of aggregating introduced the possibility of spurious results. The nonaggregated form of the network used all connections from all rats and was not easily visualizable but was more easily amenable to statistical evaluation and less likely to be biased.

To visualize connectivity maps at the group-level, connections were pooled across animals. First, we took each rat's strongest significant connection between pairs of regions and frequency bands. Because of a limited number of significant connections involving high $\gamma$, low and high $\gamma$ were combined for this analysis. Next, for connections that were significant for at least 4/5 animals, the median connectivity strength across rats was calculated. This resulted in a group connectivity matrix that was $12 \times 12$ (3 regions $\times$ 4 frequency bands). For display, these connections were plotted on a schematic of the rat brain using line thickness to indicate connectivity strength (Fig. 7, *A–D*). In addition, the group $12 \times 12$ connectivity matrix for the first open field period was used as a reference, and plots were generated to display the subset of connections that increased in strength relative to this baseline (Fig. 7, *F–H*) and decreased relative to this baseline (Fig. 7, *I–K*). Finally, the mean connectivity strength relative to baseline was also calculated between nodes within each frequency band (Fig. 7*E*), and these relative changes in connectivity strength were compared to 0 using *t* tests.

For graph-theoretic measurements on the individual rat level, each cluster was treated as a node and significant connections were treated as weighted edges. Strength, betweenness centrality, clustering coefficient, and average path length were calculated using functions from the Brain Connectivity Toolbox (25). These measures were combined across rats within each condition and sorted by strength (Fig. 7, *L–O*). The total strength within each combination of frequency band and region was summed and plotted as a heatmap for each condition (Fig. 7, *P–S*). Summed strength values were submitted to a series of within-subject ANOVAs with frequency band, region, and condition as factors. ANOVAs compared two conditions at a time: open field 1 versus novel object, open field 1 versus open field 2, open field 1 versus repeat object. *t* tests were used to assess changes in total strength in individual frequency bands.

We examined the relationship between connectivity strength and memory strength. To do this, amplitude envelope correlations were calculated on an individual session basis for connections that were significant in the group (significant at the individual level for 4/5 rats). The mean of these sessionwise connectivity values was taken for each animal. In addition, each animal's mean memory strength was calculated by taking the mean of its individual session memory strengths. Sessions with memory strength of more than 2 standard deviations from the mean were discarded from this analysis (2/28 recording sessions). Correlations were calculated between mean memory strengths and mean connectivity strengths. This analysis yielded similar results when sessions were kept separate and correlations were calculated across all 26 sessions (after removal of 2 outlier sessions).

Finally, we repeated the generation of pooled connectivity maps treating each region as a single large cluster. The same band divisions that were used in the main clustering analysis used here. The goal of this analysis was to see whether similar connectivity patterns would be discovered if the clustering process was skipped.

### Supplemental Analyses

All analyses presented here were performed on data combined from periods when the rats were moving and when they were stationary. It is known that movement can dramatically alter neural signals in rats. However, we chose to combine these behavioral states to maximize the available data for analysis. To check whether this combination may have biased results, all of the main analyses presented here were repeated with data collected during stationary periods only. This analysis largely replicated the results presented here, but where differences arose they are highlighted in the RESULTS section. The full analysis using data limited to stationary periods is available in the supplement.

## RESULTS

### Behavior

Animals were serially exposed to *1*) an empty open field, *2*) the same open field with a novel object, *3*) the empty open field again, and finally *4*) the open field with the same object. These conditions were termed open field 1, novel object, open field 2, and repeat object, respectively (Fig. 1*C*). During the open field 1 and open field 2 periods, rats tended to sit still (85% and 93% of the time, respectively; Fig. 1*F*). During the novel object and repeat object periods, rats rested for somewhat less time (84% and 90% of the time, respectively). Rats spent more time interacting with the object in the novel object than repeat object period (16% vs. 9%, respectively), but subtracting the percent of time spent interacting with the object during the repeat object period from the corresponding percentage during the novel object period did not yield a significant difference unless two visually apparent outliers were removed [after removal of outliers more than 2 SDs below mean $t(25)=4$; $P < 0.001$; Fig. 1*E*].

### Local Field Potential Power Effects

We calculated power spectra averaged across time and electrode for each behavioral condition and each brain region (Fig. 2, *B–G*). Repeated-measures *t* tests were used to compare each condition to baseline for each frequency individually. In general, spectral dynamics in all three regions were characterized by a 1/*f*-like decrease in power with increasing frequency and a peak in the θ range (5–10 Hz). The only reliable difference in the spectral profiles between behavioral conditions was a relative increase in power around 4 Hz in the STR during the novel object period.

Closer inspection of the individual power spectra per electrode revealed considerable interelectrode variability (Fig. 2, *H–M*). This suggests that the multielectrode arrays may have spanned multiple functionally distinct neural networks. We therefore proceeded to identify clusters of channels based on interchannel correlation matrices.

### Identification of Intraregional Clusters

We identified clusters of channels based on similar patterns of interchannel correlations of their LFP time series, which were identified using the DBscan algorithm (18). The clustering method was applied separately per animal, brain region, task condition, and narrowband frequency between 2 and 150 Hz, and the reliability of clusters was confirmed using 20-fold cross-validation (see METHODS for details and Fig. 3). Correlation matrices had strong block-diagonal patterns both between- and within-region, and these patterns were successfully detected and emphasized using clustering analysis (Fig. 3, *A* and *B*). Most clusters exhibited high silhouette values (19) (Fig. 3*N*). Across animals, there was a similar number of clusters detected for each condition (range 270–283 clusters over all frequencies), and the number of clusters per condition did not vary widely between animals (range 250–285). However, not all clusters survived 20-fold reliability testing.

### Cluster Reliability, Validity, and Descriptive Statistics

To ensure cluster reliability, we assessed clusters in 20 validation folds. For each fold, we repeated the clustering analysis using only 90% of the data. Clusters that were not at least 85% consistent across folds were discarded as unstable (see METHODS). This procedure led to the elimination of 13.8% of

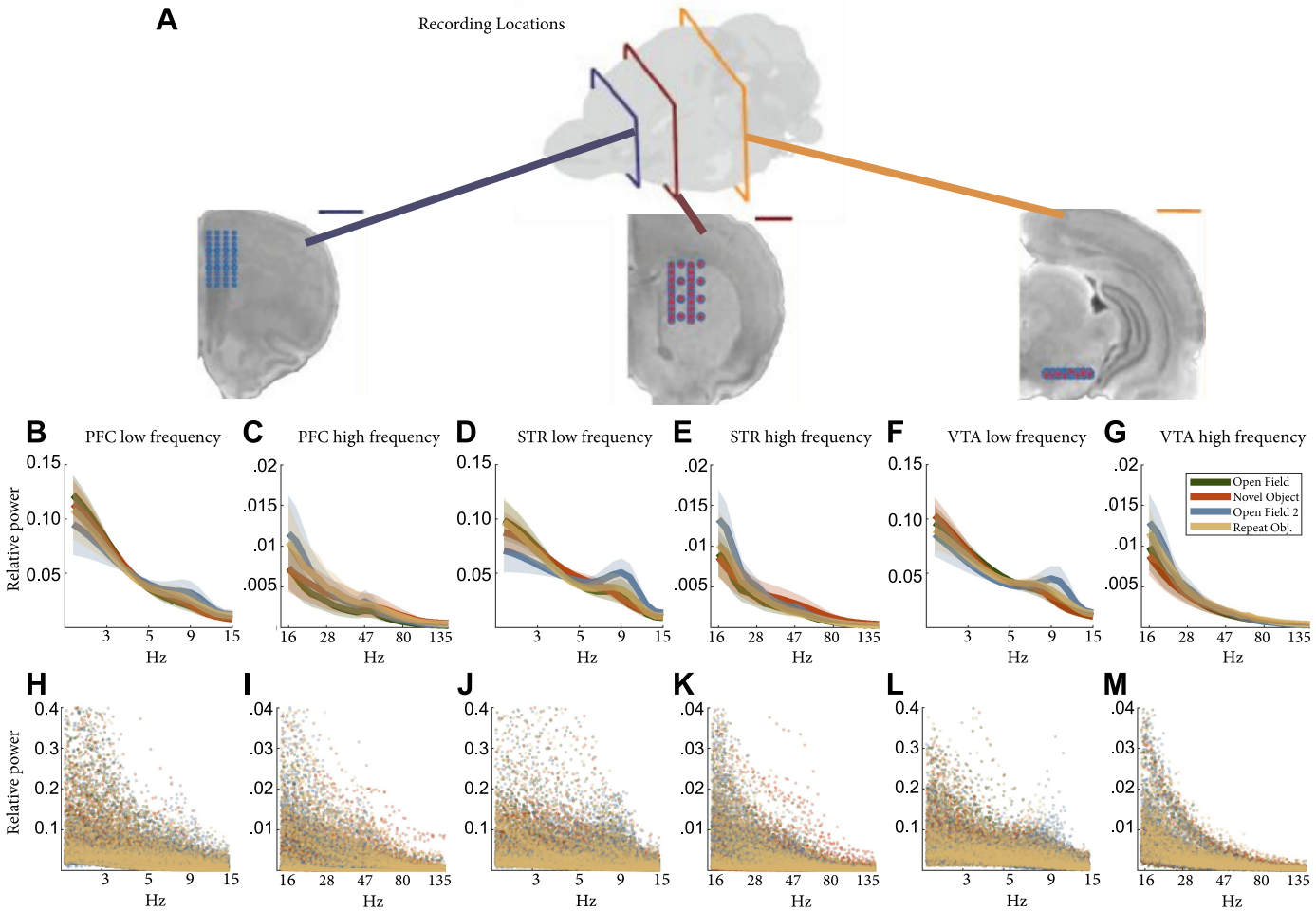


**Figure 2.** Power spectra do not differ reliably between conditions. *A*: recording locations are shown for the PFC (*left*), STR (*middle*), and VTA (*right*). Scale bars indicate 2 mm. *B–G*: group mean relative power spectra are displayed. Power spectra were calculated for each electrode. Electrode spectra were averaged and normalized to the summed spectral power across frequencies within each animal and region. Shaded regions indicate group means ± standard error. *H–M*: relative power is shown for every electrode individually, which highlights the variability in the spectra of individual: electrodes. PFC, prefrontal cortex; STR, striatum; VTA, ventral tegmental area.

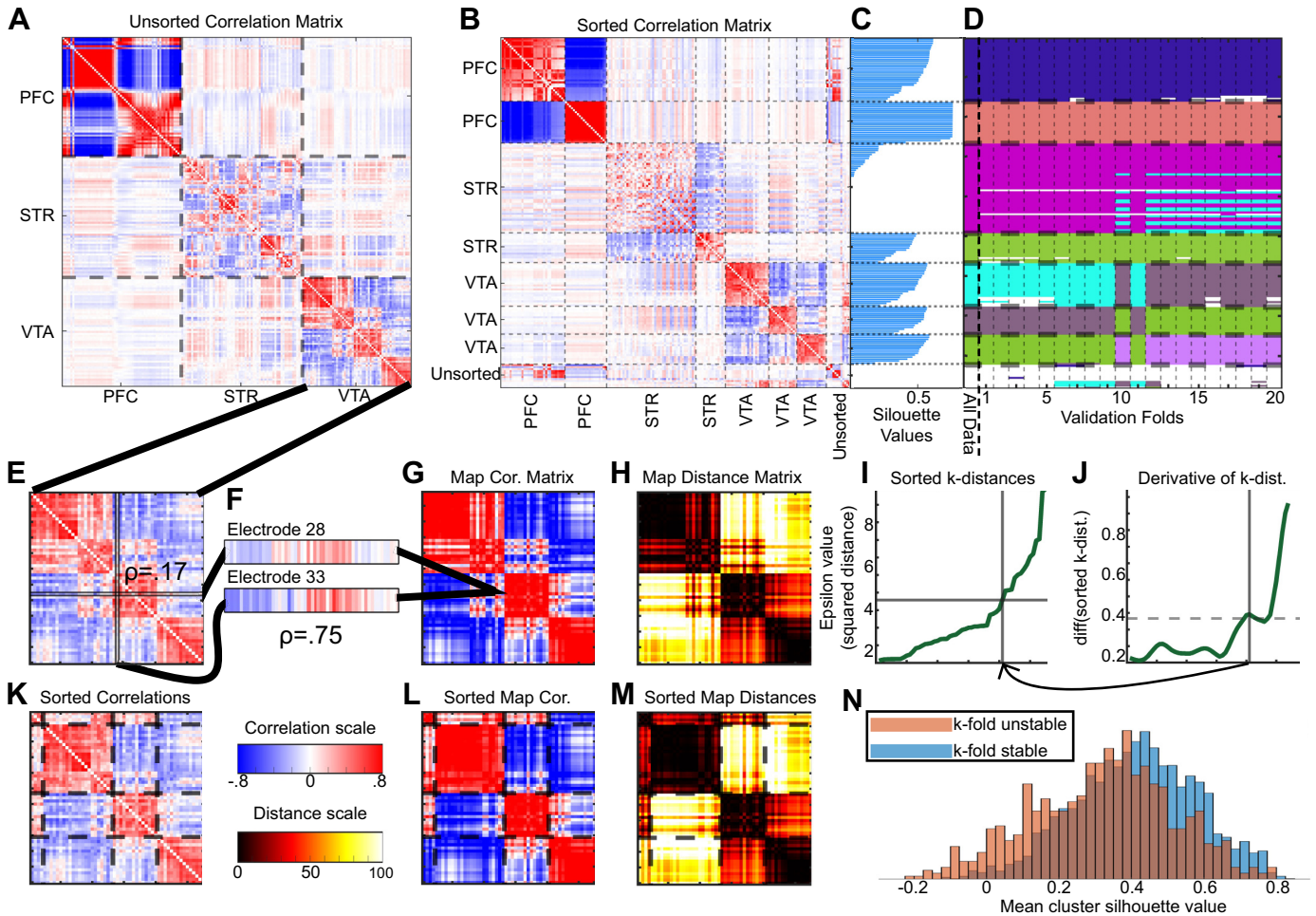


**Figure 3.** Clustering methods and validation. *A*: unsorted channel × channel correlation matrix for rat 5 during the open field period constructed using data narrowband filtered at 5.2 Hz. *B*: the same set of correlations after application of sorting pipeline. *C*: silhouette values associated with each channel. One cluster in the STR had low silhouette values, indicating poor clustering (this cluster was removed from subsequent analyses). *D*: clusters detected in "All Data" (*far left column*) and in each of 20 validation folds. Different pseudocolors indicate different clusters. The channels comprising the cluster with low silhouette values are not always clustered together, indicating instability (pink with blue stripes) (note that an entire cluster can switch colors in different folds; the important metric is whether the color is homogeneous across channels within the cluster). *E–M*: these panels display the clustering pipeline. *E*: each region's correlation matrix is considered separately. The VTA is shown here. *F*: the correlation between each row and column of the correlation matrix is calculated. Channels from electrodes 28 and 33 are displayed as examples. *G*: these correlations are organized in a matrix that encodes similarities of connectivity profiles, rather than bivariate correlations. *H:* this connectivity-profile correlation matrix was transformed into a Euclidean distance matrix to increase contrast and enforce positivity. *I*: the *k*-distance for each channel represents how far (epsilon; *y*-axis) one would have to go in units of squared distance (*H*) to find *k* nearest neighbors. *K* is set to 8. Values are sorted from smallest to largest. *J*: the derivative of the *k*-distances was approximated by taking the running difference between pairs of *k*-distances. The horizontal dashed line indicates the detection threshold for sharp discontinuity. The vertical solid line indicates a local peak. The arrow pointing back to *I* shows how the detected index in the derivative is used to select the corresponding epsilon value. This epsilon is used as input to the DBscan algorithm for clustering. *K–M*: correspond to the matrices shown in *E*, *G*, and *H*, but with channels sorted according to the result of the DBscan clustering. Cluster borders are indicated with dashed lines. *N*: mean silhouette values across electrodes in clusters that were stable across 20-fold validation (blue) and in clusters that were not stable across 20-fold validation (red). Stability was not determined using silhouette value (see METHODS), and there was no mathematical necessity that stable clusters would be expected to have higher silhouette values. PFC, prefrontal cortex; STR, striatum; VTA, ventral tegmental area.

clusters. Although we did not explicitly use silhouette values as a criterion for thresholding, eliminated clusters had lower average silhouette values than accepted clusters (Fig. 3, *D* and *N*). After 20-fold validation, there was still no marked difference in clusters per condition (range 229–247), but rat 1 exhibited fewer reliable clusters than other animals (rat 1: 199; range excluding rat 1: 238–261). The group average number of clusters summed over conditions and frequencies was not markedly different across regions (PFC: 77; STR: 76; VTA: 85.6).

Considering the narrowband signals used for clustering, the Pearson ρ values comparing channels within the same cluster were higher than those obtained when comparing channels from different clusters or that were unclustered [*t* test on animal means: $t(8)=10.7$; $P < 0.001$; Fig. 4*A*]. The mean ρ value within clusters was 0.38, and the mean value between clusters was −0.11. For 97% of cases, the average within cluster correlation was larger than the average between cluster correlation (Fig. 4*B*). For each animal × condition × region × frequency, 1,000 random cluster schemes were chosen with the same number of clusters and the same number of channels per cluster as those detected in our main analysis. Randomly chosen clusters did not exhibit a

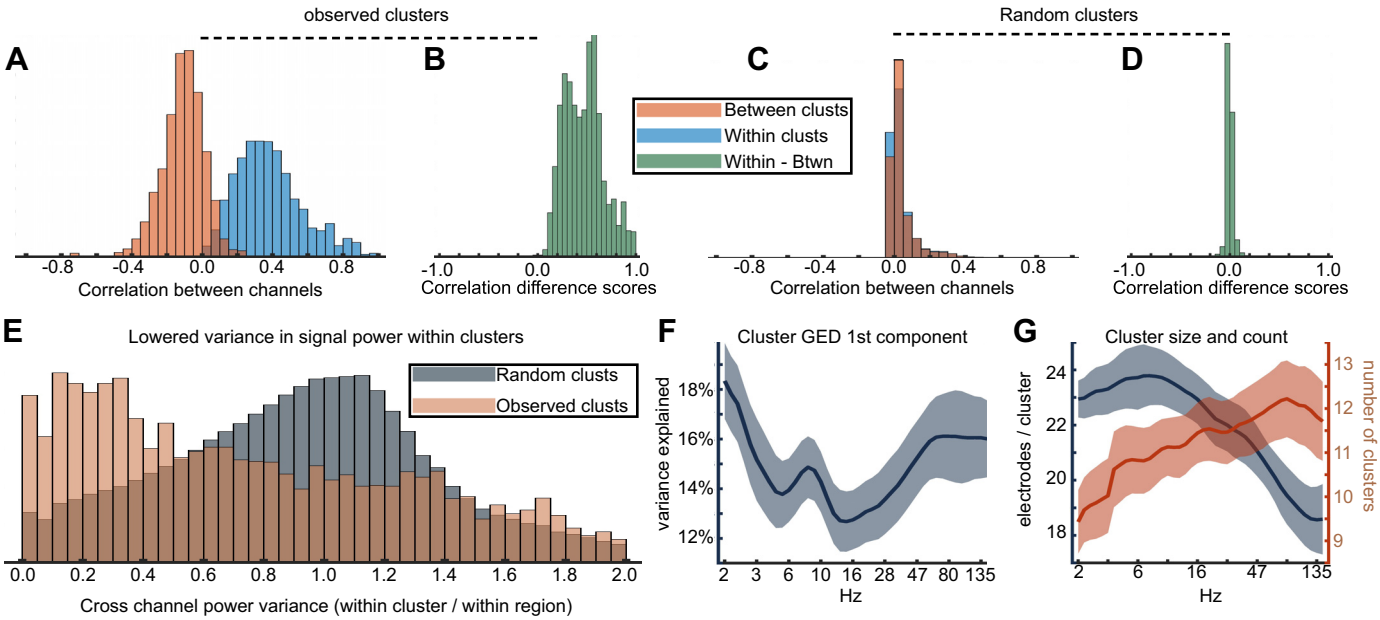


**Figure 4.** Characteristics of clusters. *A*: histograms show distributions of correlations for pairs of channels that were within the same cluster (blue) or between channels from different clusters (red). *B*: the histogram shows the distribution of difference scores calculated by subtracting between-cluster correlations from within-cluster correlations. Subtractions carried out for correlation values from the same animal, region, condition, and frequency. *C* and *D*: similar to *A* and *B*, but clusters were chosen randomly. *E*: histograms show the distributions of variance in power between channels within a cluster divided by the variance in power between channels within the corresponding region. Lower values indicate that there is less variance in power within a cluster than would be expected given the variance in its containing region. The red histogram shows the values calculated for observed clusters. The gray histogram shows the values calculated for random clusters. *F*: the first component of a generalized eigendecomposition (GED) performed on the channels within each cluster generally explained between 13% and 17% of between channel signal variance. The *y*-axis displays variance explained by the first GED component. The *x*-axis displays frequency. Higher values indicate that the entire cluster is well characterized by a single time-series. *G*: there was a larger number of smaller clusters detected at higher frequencies. The left *y*-axis displays the number of channels grouped into each cluster. The right *y*-axis displays the total number of clusters detected. The *x*-axis displays frequency. For *F* and *G*, shaded regions indicate group means ± standard error.

difference for within versus between cluster channel time-series correlations (Fig. 4, *C* and *D*).

The high correlation between channels within clusters suggested that clustering successfully detected groups of channels influenced by the same signal. To explore this further, we calculated the variance in power between channels within each cluster divided by the variance in power between all channels within each cluster's region (Fig. 4*E*). For random samples from a normal distribution, variance is insensitive to sample size, so this ratio would be expected to equal 1. Indeed, for randomly chosen clusters with the same frequency, region, and channel count characteristics as those observed, the average value for this ratio was 0.99. However, for observed clusters, the average value for this ratio was 0.83. The distributions of these power variance ratios were different (two-sample Kolmogorov–Smirnov test: $D$ = 0.24; $P \ll 0.001$). We also found that a sizable percent of the variance between channels within each cluster could be explained by a single generalized eigendecomposition (GED) component (group average between 13% and 17% across frequencies; Fig. 4*F*). Interestingly, there was a visually apparent local maximum in variance explained by the first GED component in the theta range (6–10 Hz).

Finally, the number of channels in any given cluster tended to be lower at higher frequencies, and correspondingly the number of clusters detected tended to be higher at higher frequencies (Fig. 4*G*; $\rho = -0.72$; $P \ll 0.001$). This pattern suggests that the anatomical organization of higher frequency signals is more locally differentiated than that of low frequency signals.

## Aggregating Clusters

In total, we found a mean of 238.4 statistically reliable clusters per condition across animals. Visual inspection of electrode groupings revealed that clusters were largely stable across wide ranges of frequencies (e.g., Fig. 5*D*). To assess this stability quantitatively, we calculated the normalized mutual information (NMI) (21) between cluster schemes at different frequencies and averaged the resulting NMI matrix across conditions and animals for each region (Fig. 5, *A*–*C*). Based on NMI, we utilized a greedy optimization algorithm to select divisions between frequency bands that maximized average NMI (aNMI) within bands and minimized aNMI between bands. We divided the frequency space into five bands for each region (dashed lines in Fig. 5, *A*–*C*; see METHODS). Remarkably, despite the algorithm being applied separately per region and without a priori constraints regarding the size or spectral extent of clusters, the resulting frequency bands were similar across regions and corresponded to canonical frequency bands. In the PFC and STR, the clusters mapped onto canonical δ, θ, β, low γ, and high γ (Fig. 5, *A* and *B*). By contrast, in the VTA there was a separate band for α and β was combined with low γ (Fig. 5*C*). For ease of explanation,

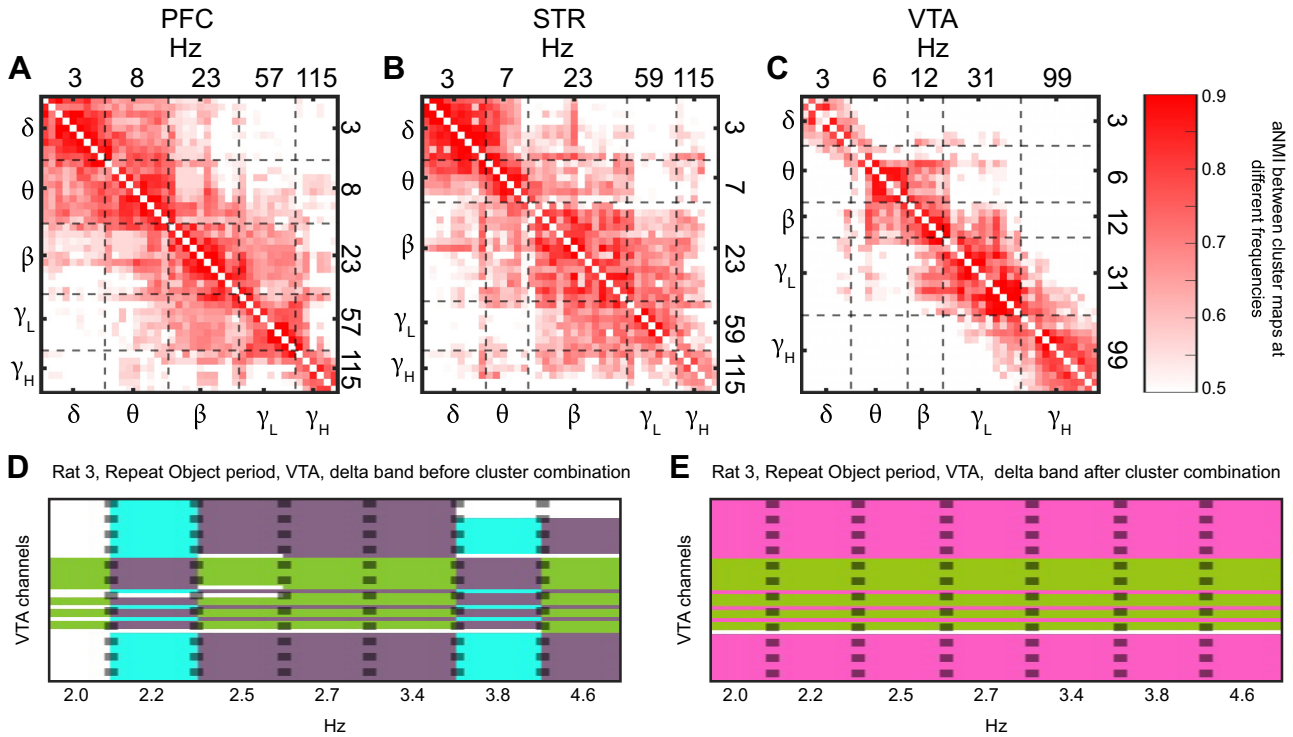


**Figure 5.** Defining frequency bands and combining clusters within bands. *A*–*C*: heat maps display the average normalized mutual information (aNMI) between cluster maps at different frequency bands. Averaging was done across rats and conditions. Dashed lines indicate the output of a greedy search algorithm that divided frequency space into bands. *Left* and *bottom* axes display band labels. *Top* and *right* axes display mean band frequency in Hz. *D* and *E*: channel-by-frequency maps illustrating the aNMI-maximizing clustering results. The *y*-axis represents channel. The *x*-axis represents frequency. Pseudo colors indicate cluster groups. *E*: a single cluster map has been constructed for all frequencies within the band such that aNMI between the final cluster map and the maps associated with the different frequencies within the band (*D*) has been maximized. PFC, prefrontal cortex; STR, striatum; VTA, ventral tegmental area.

the same band labels will be used throughout the text (see Table 2 for specific band divisions).

Next, information from different cluster schemes within each band was used to create a single cluster scheme within each band for each animal, condition, and region. To do this, we again used a greedy optimization algorithm. This time, the algorithm selected a cluster scheme that maximized the aNMI calculated across the cluster schemes within each band (Fig. 5, *D* and *E*).(21) This procedure resulted in an average of 31.5 clusters per animal in each condition.

### Changes in Within-Region Functional Structure

Clusters were detected independently within-frequency and within-condition, and the steep drop-off in aNMI values away from the diagonals in Fig. 5, *A*–*C* indicates that cluster schemes were different in different frequency bands. To quantify cluster organization similarity across behavioral conditions and frequencies, we calculated the aNMI between pairs of cluster schemes detected either within a single frequency band but between different behavioral conditions (Fig. 6, *A*–*F*), or within a single condition but between different frequency bands (Fig. 6, *G*–*M*). An aNMI near 1 indicates that network structure is very stable across either frequency or condition, and an aNMI near 0 indicates that network structure is very different across either frequency or condition.

In general, aNMI values were higher than would be expected by chance but also consistently below 1, meaning that internal network structure in the PFC, STR, and VTA was neither completely remapped or completely stable either when looked at across different conditions (Fig. 6, *A*–*F*) or across different frequencies (Fig. 6, *G*–*M*). More specifically, for every paired combination of animal, condition, region, and frequency, we generated 1,000 random pairs of cluster schemes where the total number of channels, the number of clusters, and the number of channels per cluster were held constant. aNMI between these pairs was calculated. The 99th percentile of these random distributions is plotted in Fig. 6 (dashed lines). Random restructuring led to a maximum aNMI of ~0.2 across all situations. Yet, we observed aNMI values that were consistently higher than this.

To examine remapping between different conditions, we calculated the aNMI of cluster schemes within frequency between different conditions. Separately for each condition, this analysis captures the average similarity of a condition

**Table 2.** *Divisions between frequency bands, values in Hz*

| Region | Delta (δ) | Theta (θ) | Beta (β) | Gamma Low (γL) | Gamma High (γH) |
|---|---|---|---|---|---|
| PFC | 2–4.6 | 4.6–12.0 | 12.0–34.3 | 34.3–79.4 | 79.4–150 |
| STR | 2–4.6 | 4.6–8.7 | 8.7–38.2 | 38.2–79.4 | 79.4–150 |
| VTA | 2–3.8 | 3.8–8.8 | 8.8–14.8 | 14.8–47.1 | 47.1–150 |

PFC, prefrontal cortex; STR, striatum; VTA, ventral tegmental area.

with the other three conditions while holding the frequency constant. For example, considering only clusters observed in the δ band in the VTA and averaging across animals, the NMI of the cluster organization observed during the open field 2 period had similarities of 0.51, 0.25, and 0.35 with the clusters observed during open field 1, novel object, and repeat object periods, respectively. Averaging these three values yielded 0.37 which is displayed in Fig. 6*E*. aNMI values were submitted to a 5 (frequency bands) × 4 (conditions) within-subjects ANOVA for each region (the ANOVA numerical data are presented in Supplemental Table S1; here we highlight only the relevant significant results). In the PFC

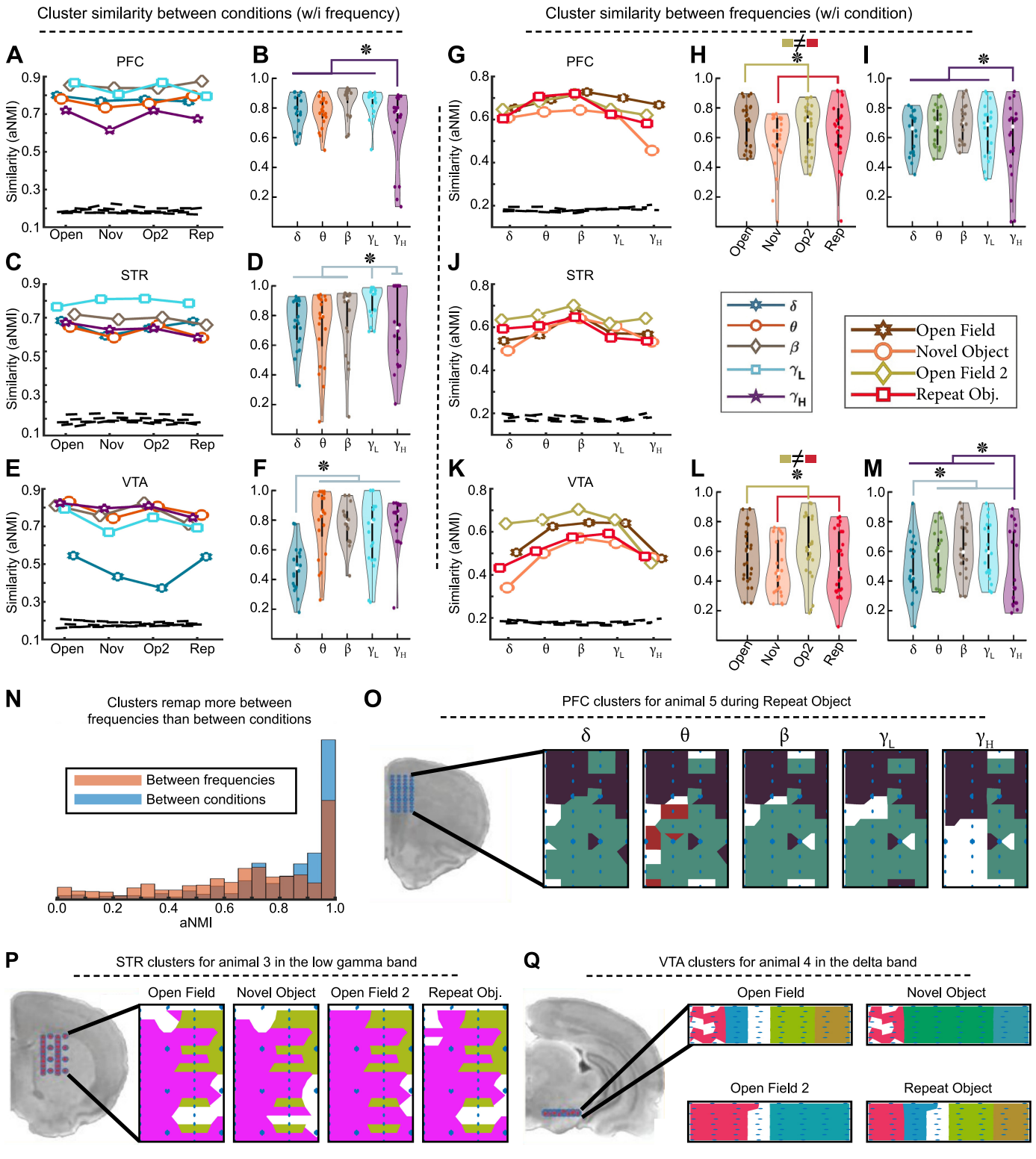

there was a main effect of frequency (Fig. 6, *A* and *B*). Visual inspection of Fig. 6*A* indicated that this effect was driven by reduced cross-condition stability in high γ, and this was confirmed by linear contrast. But it appears that a small number of data points drove the effect (Fig. 6*B*). In the STR, there was also a main effect of frequency (Fig. 6, *C* and *D*), and this was driven by relatively high stability in the low γ band (Fig. 6*D*) as well as low stability in the θ band (not shown). The effects in the PFC and STR were relatively modest ($\eta^2 < 0.2$). By contrast, the VTA exhibited dramatic remapping of its cluster structure in the δ band (Fig. 6, *E* and *F*; $\eta^2 = 0.48$). Taken together, the STR was generally stable across conditions in all frequency bands. The PFC exhibited moderate restructuring of its cluster structure in the high γ band, and the VTA restructured dramatically across behavioral states, but this restructuring was limited to δ band signaling.

To examine independence between different frequencies, we again used aNMI. Separately for each frequency, this analysis captures the average similarity of cluster organization in one frequency band with the other four frequency bands while holding condition constant. These aNMI values were submitted to a 5 (frequency bands) × 4 (conditions) within-subject ANOVA for each region (for ANOVA table see Supplemental Table S2). In the PFC, there were main effects of both frequency and condition (Fig. 6, *G–I*). These effects were driven by lower cross-frequency cluster scheme similarity in behavioral periods with an object present (both novel object and repeat object periods; Fig. 6*H*) and lower cross-frequency similarity in the cluster structure of high γ signaling relative to other frequency bands (Fig. 6*I*). There were no significant effects in the STR (Fig. 6*J*). In the VTA, there were main effects of both frequency and condition (Fig. 6, *K–M*). As in the PFC, behavioral periods with objects had lower cross-frequency cluster structure similarity than those without an object (Fig. 6*L*). Also similar to the PFC, the cluster scheme for high γ was dissimilar from the cluster schemes of other frequency bands. In addition, and unlike the PFC, the cluster structure of δ signaling was dissimilar to other frequency bands in the VTA (Fig. 6*M*).

Taking these two analysis approaches together, PFC high γ and VTA δ exhibited significant changes in cluster schemes. This indicates that these areas remap their internal structures with respect to signaling in these frequency bands across conditions (for single animal example see Fig. 6*Q*) and that the physical layout of signaling in these frequency bands is different from other frequency bands (for single animal example see Fig. 6*O*). Furthermore, both regions exhibit more cross-frequency dissimilarity in the object periods, suggesting a greater degree of functional segregation between frequency-specific signal generators during object interaction. By contrast, the STR exhibited relatively high stability across conditions (for single animal example see Fig. 6*P*). Finally, it is clear from visual examination of Fig. 6 that cluster structures are generally more differentiated between different frequencies than across different conditions, suggesting independence of the neural substrates supporting signaling in different frequency bands. Averaging across animals, conditions, regions, and frequencies, within-frequency aNMI values had a mean of 0.82 (Fig. 6, *A–F*), but within condition aNMI values had a mean of 0.68 [Fig. 6, *G–M*; $P \ll 0.001$; confidence interval (CI): 0.12–0.16; see histogram in Fig. 6*N*]. That said, it should be emphasized that the most striking intraregional cluster differences were observed within the delta frequency band in the VTA, suggesting that this structure remapped dramatically with respect to delta-band signal generation.

### Between-Region Network Structure

As mentioned earlier, using GED to reduce the dimensionality of cluster signals to a single time course generally yielded a component that explained a sizable portion of the variance between channels (Fig. 4*F*). After converting each cluster into a single time course, we examined connectivity between clusters using amplitude envelope correlations (14). A bootstrapped null distribution was constructed for each connection (see METHODS). Correlations were considered significant if they were stronger than 95% of their corresponding null correlations. The results of this procedure can be thought of as connectivity graphs for each animal in each condition. In these graphs, each node was a cluster with a specific region and frequency band, and edges were the correlations between nodes. Because there were often multiple clusters with the same region and frequency band, animals could sometimes have multiple connections along the same edge. To aggregate connections across animals, the strongest significant correlation between each frequency, region pair

**Figure 6.** Intra-regional cluster stability. *A–F*: average normalized mutual information (aNMI) calculated across conditions but within frequency band. *A*: PFC aNMI values (*y*-axis) are displayed for the four conditions (*x*-axis). Each line indicates results for a different frequency band (legend is next to *J*). Dashed lines indicate expected values in an analysis of random clusters. There was a main effect of frequency [$F(4,76) = 4.13$; $P < 0.01$]. *B*: PFC aNMI values were grouped by frequency band. Violin plots show aNMI values (*y*-axis) for condition similarity per frequency (*x*-axis). Each animal is represented by 4 dots (one for each condition) for each frequency. *C* and *D:* similar to *A* and *B* except for the STR. There was a main effect of frequency [$F(4,76)=3.67$; $P = 0.01$]. *E* and *F:* similar to *A* and *B* except for the VTA. There was a main effect of frequency [$F(4,76)=17.6$; $P \ll 0.01$]. δ had lower aNMI than other frequency bands. *G–M*: aNMI calculated across frequencies but within condition. *G*: PFC aNMI values (*y*-axis) are displayed for the five frequency bands (*x*-axis). Each line indicates results for a different condition. There were main effects of condition and frequency (*F* values > 3.7; *P* values < 0.02). *H:* PFC aNMI was grouped by condition. Violin plots show aNMI values (*y*-axis) for frequency similarity calculated within each condition (*x*-axis). Each animal is represented by 5 dots (one for each frequency) for each condition. *I:* PFC aNMI was grouped by frequency, generating a plot similar to *B*, except the underlying calculation here was within condition instead of within frequency. *J*: similar to *G* for data from the STR. There were no significant main effects for the STR. *K–M*: similar to *G–I* for data from the VTA. There were main effects of condition and frequency (*F* values > 9; *P* values ≪ 0.01). *N*: histogram shows aNMI in the between frequency (red) and between condition (blue) analyses. Between-frequency comparisons generally had lower aNMI. *O–Q*: examples of cluster remapping. Anatomical location of recording array is shown to the *left* and clusters are mapped to anatomical space in panels to the *right*. Pseudo colors indicate different clusters (unassigned electrodes have no color). *O*: this example shows that high γ in the PFC had a cluster scheme different from the other bands (see also lower aNMI values in *I*). *P:* clusters in the low γ band in the STR. Note the stability in cluster organization across conditions (see also *D*). *Q:* this example demonstrates the effect observed in *E*. Namely, δ in the VTA had an unstable cluster map across conditions. Asterisks indicate significant linear contrasts in an ANOVA model. Please see Supplemental Tables S1 and S2 for complete statistics. PFC, prefrontal cortex; STR, striatum; VTA, ventral tegmental area.

was taken for each animal. Any edge that did not have at least one significant connection for 4/5 rats was discarded. The medians of these maximum connection strengths across animals in each condition are plotted in Fig. 7, *A–D*. There were few significant connections including high γ, so these connections were grouped with low γ for this analysis. In general, the pattern of connectivity was dense in the first open field period, with 72% of all possible connections

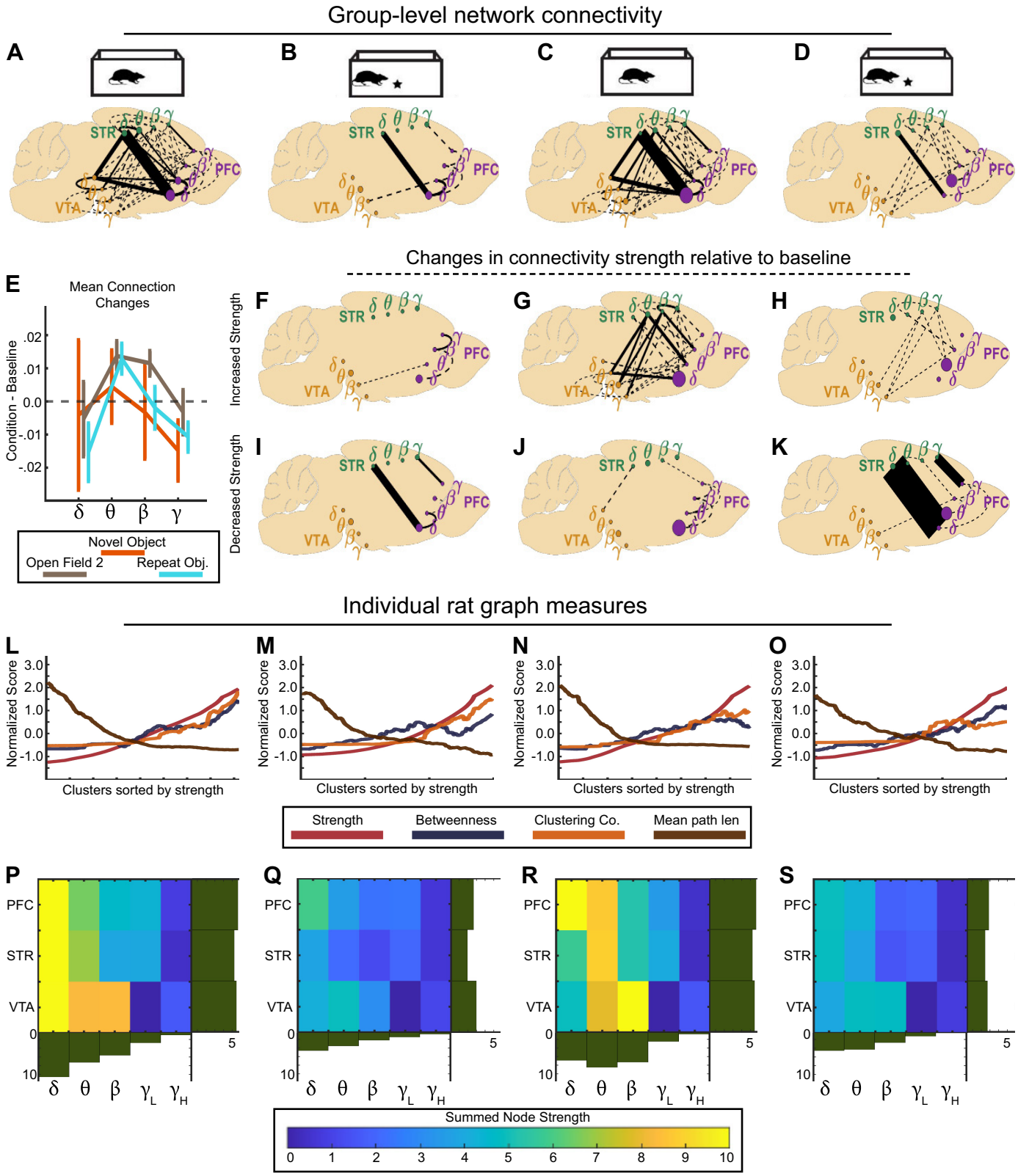

exhibiting significant coupling. Connectivity dropped during the novel object period, with 2% of all possible connections exhibiting significant strength. Connectivity then rebounded in the second open field period to 52%, and then fell again during the repeat object period to 18%. In addition, while PFC δ was the node with the highest betweenness centrality in the first three behavioral conditions, PFC θ became the node with highest betweenness in the repeat object period (dot size in Fig. 7, *A–D*).

To unpack these results further, we replotted the connectivity as a function of change relative to connectivity strength during the first open field period (Fig. 7, *F–H* for increases; Fig. 7, *I–K* for decreases). In general, connections in the θ band strengthened marginally during the second open field and repeat object periods (Fig. 7*E*; $P$ values $<$ 0.07). In addition, there was also β band connection strengthening in the second open field period ($P$ = 0.0503), but this result became nonsignificant when the analysis was limited to stationary periods only. This suggests that θ and β connections strengthened markedly in movement periods, but there was insufficient data to carry out an analysis limited to movement period alone. In the repeat object period, a complex pattern of high frequency interactions involving the β and γ bands emerged (Fig. 7*H*). Interestingly, decreases in specific δ band connections between regions were observed in all three conditions, but these were not significant in the aggregate (Fig. 7*E*).

To check whether the aggregating process had biased the results, we calculated graph theoretic descriptive statistics on the full cluster × cluster connectivity matrices of significant connections derived for each rat. In general, nodes with high strength also had high betweenness, high clustering coefficients, and low path lengths (Fig. 7, *L–O*). We summed the strength of all clusters within each region and frequency band (Fig. 7, *P–S*). The results observed in the aggregated graphs were recapitulated. Overall strength reduced markedly in the object periods relative to the open field periods. In addition, while strength was concentrated in the δ band during the first open field period (Fig. 7*P*), θ band connections exhibited the most strength during the second open field period (Fig. 7*R*). These results were confirmed with a series of within-subject ANOVAs comparing pairs of conditions using frequency band, condition, and region as factors (for full ANOVA tables see Supplemental Tables S3, S4, and S5). Confirming the overall drop in strength during the object periods, there was a main effect of condition in comparisons between the first open field period and novel object periods and between first open field and repeat object periods [$F$ values (1,281) $>$ 114; $P$ values $\ll$ 0.001], but this main effect was absent when comparing the two open field periods to each other ($P$ = 0.8). Confirming the shift from δ to θ strength, there was an interaction between condition and frequency for comparisons between the first open field period and all three other conditions [$F$ values (4,281) $>$ 8.8; $P$ values $\ll$ 0.001]. Comparisons targeted at examining changes in relative δ/θ strength found that δ band connections were weaker in the second open field period relative to the first open field period [$t$(58) = −3.3; $P$ = 0.002], and connection strength in the θ band was marginally increased during the second open field period relative to the first open field period [$t$(60) = 1.9; $P$ = 0.055]. However, although δ band decreases were robust when analysis was limited to stationary periods, θ band increases were not (see *Supplemental Analyses*).

We considered whether inter-regional connections played a role in memory. To test for this, connectivity strength of all significant connections was calculated for each session independently. Memory strength for each session was assessed as shown in Fig. 1*E*. For each animal, we took the mean connection strength and memory strength values across sessions and then calculated the correlation between these values. Interestingly, during the second open field period, θ connections between the VTA and STR and between the VTA and PFC were significantly correlated with memory ($P$ values $<$ 0.05; Supplemental Fig. S7-1). However, a correlation analysis with only five animals should be interpreted with an appropriate amount of caution.

Finally, to check whether clustering had meaningfully contributed to our network connectivity findings at all, we repeated the GED and connectivity analysis considering entire regions as singular clusters (Supplemental Fig. S7-2). In general, this analysis found markedly fewer significant connections. In particular, only three connections were found in the repeat object period when entire regions were considered, compared with 26 connections observed using clusters. In other words, segregating the intraregional activity into clusters was crucial to uncovering many of the functional dynamics reported here.

## DISCUSSION

We found that network dynamics exhibited a complex pattern of changes in inter-regional functional connectivity

**Figure 7.** Dynamics of inter-regional connectivity across behavioral epochs. *A–D*: group mean correlations between signals derived from frequency-specific regional clusters are shown as line thickness. Stars indicate the presence of an object to explore (novel object and repeat object periods). Solid lines range from ρ = 0.05 to ρ = 0.20. Dashed lines represent weaker connections (ρ $>$ 0.0). All visualized connections were significant at the individual level for at least 4/5 animals. Each animal contributed only its strongest single connection to each graph edge. Node size represents betweenness centrality. These connection strengths are reused in *E–K*. *E*: group mean change relative to open field in connection strength for connections between nodes within different frequency bands. Inter-regional connections in the θ band had marginally increased strength in the open field 2 and repeat object periods ($t$ test against 0, $P$ values $<$ 0.07). Connections in the β band had increased strength in the open field 2 period ($P$ = 0.0503). *F–H*: specific connections that exhibited increased strength relative to open field in the novel object (*F*), open field 2 (*G*), and repeat object (*H*) periods. *I–K*: similar to *F–H* but for decreased strength connections. Throughout *F–K*, solid lines represent connectivity changes of between ρ = 0.0125 and ρ = 0.07. Dashed lines represent weaker connections (ρ $>$ 0.0). *L–O*: graph theoretic measurements of each animal's connectivity matrix were calculated for all significant connections (rather than taking only each animal's strongest edge between any two nodes). Metrics were $z$-scored for display on a single scale. Node-metrics from all animals were combined and sorted by strength for plotting. In general, nodes with high strength also had high betweenness centrality, high clustering coefficients, and low mean path lengths. *P–S*: summed strength values of all nodes in different regions ($y$-axis) and within different frequency bands ($x$-axis). Marginal histograms display the mean value of their respective rows or columns of the heatmap. Overall node strength was lower in the novel object and repeat object periods (*Q* and *S*), and the frequency of peak nodal strength shifted from δ to θ when comparing open field (*P*) to open field 2 (*R*). Please see Supplemental Tables S3–S5 for complete statistics.

(Fig. 7) and intraregional signal distribution (Fig. 6). During the first open field period, we observed that the STR, PFC, and VTA were robustly connected across multiple frequency bands, with δ oscillations playing an outsized role. There was a dramatic pruning of network connectivity when rats were exposed to a novel object. After the novel object was removed, connectivity rebounded during the second open field period, but the connectivity profile shifted away from being dominated by δ. Finally, when animals were re-exposed to objects, connections were not as severely reduced as they had been during initial presentation, and specifically θ and higher-frequency connections were stronger than they had been during the novel object period. Underlying these inter-regional changes, functional organization of γ frequency signals in the PFC and both γ and δ signals in the VTA all changed markedly across behavioral conditions.

It is important to appreciate that these patterns were detectable only with the use of subregional clustering analysis (Supplemental Fig. S3). Although there was considerable variability in the signals recorded at different electrodes (Fig. 2), we found that subregional clusters of electrodes were stable across multiple sessions recorded on different days. These clusters were verified using 20-fold validation, silhouette value examination (Fig. 3), and by comparing the statistics of observed clusters to those of randomly chosen clusters (Fig. 4). In general, clusters covered between a quarter and a third of the space of our electrode arrays (mean cluster size 18–24 electrodes; Fig. 4*G*). Thus, for the STR and PFC, clusters covered an area of approximately half a square millimeter, and, in the VTA, they covered less than a tenth of a square millimeter. These areas are smaller than the traditional demarcations between architectonically categorized brain regions (28). This highlights the rich pattern of fine-grained spatiotemporal dynamics that can be discovered only through large-scale recordings and multivariate data analyses. Of practical importance, the finding that changing subregional signal generators can give rise to changing network connectivity raises the possibility that previous studies of network connectivity may have averaged functionally different signals together, obscuring meaningful connections.

The idea that such small areas could act as functionally important units in long distance patterns of connectivity is consistent with principles of anatomy: anatomical tract tracing studies have often found exquisite patterns such that regions lying only a single millimeter apart can have dramatically different profiles of connectivity (29), and the patterns of connectivity between our three recording targets are no exception (30–33). Recent work has begun to reveal the functional importance of highly specific anatomy. For example, in rodents, specific fiber pathways are independently responsible for dopamine-dependent learning about novel objects and social stimuli in the VTA (34). In monkeys, connectivity between small cortical patches supports face perception (35–37). In humans, distinct subfields within the VTA are important for novelty and reward detection, and each of these subfields exhibits a unique pattern of functional connectivity (38). The present results help to generalize these findings further, showing how subregional patches of brain tissue form changing patterns of long-distance connectivity even when two periods of minimally different open field data are compared and during novel and repeated object interaction.

In addition, we observed that signals at different temporal frequencies and signals measured during different behavioral conditions both had distinct cluster topographies (Fig. 6). This suggests that frequency-specific signal generators are anatomically localized and can be activated or deactivated depending on task demands, resulting in a constantly shifting landscape of functional anatomy. This finding also builds on earlier work. For example, in humans the BOLD activation associated with semantic concepts changes across the entire cortical mantle in response to attentional goals (39), and nodes of the default mode network become less connected during cognitively engaging tasks (40). More generally, Honey et al. (5) used a computational model of biologically inspired brain signals and known anatomical connectivity of the macaque brain to simulate electrophysiology data. They found that functional connectivity simulated over a long time window (minutes) recapitulated patterns of anatomical connectivity, but on shorter time scales (seconds or less) patterns of functional connectivity deviated from the model's set anatomy. The authors interpreted this finding to mean that the brain is capable of dynamically changing its functional connectivity in ways that would not be predicted from anatomy alone, and our results confirm this interpretation. However, Honey et al. (5) reported that functional connectivity exhibits regression toward the mean over relatively short periods of time (10 s of seconds). By contrast, we observed sustained periods with dramatically different cluster structures and long-distance connectivity, implying that both local and global network states can be held far from any equilibrium for at least several minutes in response to environment/task changes. As discussed by Honey et al. (5), computational modeling efforts with explicit consideration of context may capture this phenomenon.

Examining the specific pattern of connectivity changes exhibited in the present results, the lack of inter-regional connectivity during the novel object period is striking (Fig. 7, *B* and *Q*). This result is surprising considering the vigorous novelty response produced by dopamine neurons of the VTA in both cats and monkeys (41, 42) and the finding that dopamine (DA) antagonists can impair memory in rodents (43). In humans, dopaminergic single-unit firing in the substantia nigra has been shown to predict subsequent memory for novel stimuli (44). Although we did not explicitly test memory, it is likely that rats formed incidental memories of the objects encountered in the experiment. This may be reflected in their decreased exploration of the objects during the repeat object period (Fig. 1*E*). The seeming paradox of the known importance of DA in novelty signaling, juxtaposed with our observation of a disconnected VTA, could be explained by a connection between the VTA and an area that we did not record from. Much work has implicated the interaction between the hippocampus (HPC) and VTA in response to novelty and memory encoding (45). For example, fMRI data have revealed a novelty signal in the VTA associated with connectivity to the HPC, nucleus accumbens, and primary visual cortex (38). The primary role for the HPC in the early stage of novelty encoding is further supported by faster neural response times for memory-

predicting firing in the HPC compared with the substantia nigra in humans (44). Our data extend this finding by showing that other connections involving the VTA and important memory structures are suppressed during novelty encoding, heightening the importance of any HPC-VTA connection.

A second point of interest was the shift away from δ (~4 Hz) connectivity during the first open field period to possible θ (~8 Hz) connectivity during the later periods (Fig. 7, *E, P,* and *R*). There have been many reports highlighting coherent θ oscillations linking the HPC and PFC during declarative memory tasks (27, 44–47), and putative DA cells in the midbrain of humans exhibit spiking coherence with PFC theta that is memory-dependent (44). By contrast, during a stimulus-response association task, δ frequency synchrony between the HPC, PFC, and VTA was interpreted as influence from the STR (48). This interpretation was based on prior observations of δ oscillations in the STR during this type of task. Although Fujisawa and Buzsaki (48) demonstrated that the HPC can be influenced by δ oscillations in a network involving the PFC and the VTA, our data demonstrate the reverse: delta oscillations can be suppressed in a network involving the PFC and the VTA. Taken together, this may indicate that changes in dominant frequency and connectivity may be as important as changes in the overall level of involvement of different areas in different tasks. For example, procedural memory may be productively thought of as involving δ signaling in an extended memory network rather than as dependent on the STR, and declarative memory may be thought of as θ signaling within the same extended network rather than as dependent on the HPC alone. Indeed, there was some evidence that θ connections between the VTA and the other two structures during the second open field period were related to decreases in object exploration between the novel and repeat object periods (Supplemental Fig. S7-1). However, Fujisawa and Buzsaki's experiment utilized a very different behavioral task and analysis approach, making direct comparisons difficult.

At a subregional level, the most dramatic remapping of cluster structure was observed in δ-band signaling in the VTA. By contrast, the STR exhibited the least remapping of the three structures from which we recorded (Fig. 6). These findings contribute to a growing literature that suggests the VTA and dopamine signaling may coordinate the interplay between the HPC and the STR (26, 44–46, 48–50). In this context, a prediction from our results is that the HPC and VTA would be expected to exhibit strong connectivity in response to novelty and that this connectivity should be related to both the δ frequency remapping of the VTA and any memory-associated projection of θ frequency signaling from the VTA to the STR and PFC.

Finally, we observed a complex pattern of higher frequency connections during the repeat object period that were not present during the novel object period. It is widely accepted that memory retrieval involves a network of activation, and this is particularly true of old memories (51). Our data indicate that some network connections needed to support retrieval may be formed within minutes of initial encoding.

Three major limitations of this study are the need to relate the local clustering and global connectivity to single-unit firing, our lack of measurement of potentially involved structures beyond the STR, VTA, and PFC (primarily the hippocampus), and the need for more robust behavioral tests of memory. We believe these areas present important avenues for future work to extend the results presented here.

In conclusion, network state can change dramatically after even minimal behavioral perturbation. Inter-regional network changes depend on underlying changes in the anatomical extent of functional signal generators at the subregional level. This implies a complex interplay between changes at micro- and mesoscale levels. Future studies will likely benefit from consideration of changes in subregional signal generators when examining network connectivity between regions.

## DATA AVAILABILITY

The data that support the findings of this study are available from the corresponding author upon reasonable request.

## CODE AVAILABILITY

Key custom functions are available on Github (https://github.com/adede1988/subNetworkDynamics). Full processing scripts are available from the corresponding author upon reasonable request.

## SUPPLEMENTAL DATA

Supplemental figures and analyses are available in the same Github repository (https://github.com/adede1988/subNetworkDynamics) as the code.

## GRANTS

M.X.C. was funded by an ERC-StG 638589. N.M. and P.M.A. were funded by a Hypatia award from the Radboud University Medical Center to M.X.C. A.J.O.D. was funded by the Unit of Excellence on Clinical Outcomes Research and Integration grant.

## DISCLOSURES

No conflicts of interest, financial or otherwise, are declared by the authors.

## AUTHOR CONTRIBUTIONS

A.M., N.M., R.R., P.M.A., and M.X.C. conceived and designed research; A.M., N.M., R.R., and P.M.A. performed experiments; A.J.O.D. analyzed data; A.J.O.D. and M.X.C. interpreted results of experiments; A.J.O.D. prepared figures; A.J.O.D. drafted manuscript; A.J.O.D., A.M., N.M., R.R., P.M.A., and M.X.C. edited and revised manuscript; A.J.O.D., A.M., N.M., R.R., P.M.A., and M.X.C. approved final version of manuscript.

## ENDNOTE

At the request of the authors, readers are herein alerted to the fact that additional materials related to this manuscript may be found at https://github.com/adede1988/subNetworkDynamics. These materials are not a part of this manuscript and have not undergone peer review by the American Physiological Society (APS). APS and the journal editors take no responsibility for these materials, for the website address, or for any links to or from it.

## REFERENCES

1. **Jensen O**, **Mazaheri A.** Shaping functional architecture by oscillatory alpha activity: gating by inhibition. *Front Hum Neurosci* 4: 186, 2010. doi:10.3389/fnhum.2010.00186.

2. **Singer W.** Distributed processing and temporal codes in neuronal networks. *Cogn Neurodyn* 3: 189–196, 2009. doi:10.1007/s11571-009-9087-z.
3. **Wang X-J.** Neurophysiological and computational principles of cortical rhythms in cognition. *Physiol Rev* 90: 1195–1268, 2010. doi:10.1152/physrev.00035.2008.
4. **Bastos AM**, **Vezoli J**, **Bosman CA**, **Schoffelen J-M**, **Oostenveld R**, **Dowdall JR**, **De Weerd P**, **Kennedy H**, **Fries P.** Visual areas exert feedforward and feedback influences through distinct frequency channels. *Neuron* 85: 390–401, 2015. doi:10.1016/j.neuron.2014.12.018.
5. **Honey CJ**, **Kötter R**, **Breakspear M**, **Sporns O.** Network structure of cerebral cortex shapes functional connectivity on multiple time scales. *Proc Natl Acad Sci USA* 104: 10240–10245, 2007. doi:10.1073/pnas.0701519104.
6. **Honey CJ**, **Sporns O**, **Cammoun L**, **Gigandet X**, **Thiran JP**, **Meuli R**, **Hagmann P.** Predicting human resting-state functional connectivity from structural connectivity. *Proc Natl Acad Sci USA* 106: 2035–2040, 2009. doi:10.1073/pnas.0811168106.
7. **de Pasquale F**, **Della Penna S**, **Snyder AZ**, **Lewis C**, **Mantini D**, **Marzetti L**, **Belardinelli P**, **Ciancetta L**, **Pizzella V**, **Romani GL**, **Corbetta M.** Temporal dynamics of spontaneous MEG activity in brain networks. *Proc Natl Acad Sci USA* 107: 6040–6045, 2010. doi:10.1073/pnas.0913863107.
8. **Hipp JF**, **Hawellek DJ**, **Corbetta M**, **Siegel M**, **Engel AK.** Large-scale cortical correlation structure of spontaneous oscillatory activity. *Nat Neurosci* 15: 884–890, 2012. doi:10.1038/nn.3101.
9. **Vezoli J**, **Vinck M**, **Bosman CA**, **Bastos AM**, **Lewis CM**, **Kennedy H**, **Fries P.** Brain rhythms define distinct interaction networks with differential dependence on anatomy. *Neuron* 109: 3862–3878.e5, 2021. doi:10.1016/j.neuron.2021.09.052.
10. **Brookes MJ**, **Woolrich M**, **Luckhoo H**, **Price D**, **Hale JR**, **Stephenson MC**, **Barnes GR**, **Smith SM**, **Morris PG.** Investigating the electrophysiological basis of resting state networks using magnetoencephalography. *Proc Natl Acad Sci USA* 108: 16783–16788, 2011. doi:10.1073/pnas.1112685108.
11. **Bassett DS**, **Sporns O.** Network neuroscience. *Nat Neurosci* 20: 353–364, 2017. doi:10.1038/nn.4502.
12. **Khambhati AN**, **Sizemore AE**, **Betzel RF**, **Bassett DS.** Modeling and interpreting mesoscale network dynamics. *NeuroImage* 180: 337–349, 2018. doi:10.1016/j.neuroimage.2017.06.029.
13. **Khambhati AN**, **Mattar MG**, **Wymbs NF**, **Grafton ST**, **Bassett DS.** Beyond modularity: Fine-scale mechanisms and rules for brain network reconfiguration. *NeuroImage* 166: 385–399, 2018. doi:10.1016/j.neuroimage.2017.11.015.
14. **Bruns A**, **Eckhorn R**, **Jokeit H**, **Ebner A.** Amplitude envelope correlation detects coupling among incoherent brain signals. *Neuroreport* 11: 1509–1514, 2000.
15. **Mishra A**, **Marzban N**, **Cohen MX**, **Englitz B.** Dynamics of neural microstates in the VTA-striatal-prefrontal loop during novelty exploration in the rat. *J Neurosci* 41: 6864–6877, 2021. doi:10.1523/JNEUROSCI.2256-20.2021.
16. **Mathis A**, **Mamidanna P**, **Cury KM**, **Abe T**, **Murthy VN**, **Mathis MW**, **Bethge M.** DeepLabCut: markerless pose estimation of user-defined body parts with deep learning. *Nat Neurosci* 21: 1281–1289, 2018. doi:10.1038/s41593-018-0209-y.
17. **Liu X**, **Zhu X-H**, **Qiu P**, **Chen W.** A correlation-matrix-based hierarchical clustering method for functional connectivity analysis. *J Neurosci Methods* 211: 94–102, 2012. doi:10.1016/j.jneumeth.2012.08.016.
18. **Ester M**, **Kriegel H-P**, **Sander J**, **Xu X.** A density-based algorithm for discovering clusters in large spatial databases with noise. In: *Proceedings of the 2nd International Conference on Knowledge Discovery and Data Mining*. Palo Alto, CA: AAAI Press, 1996, p. 226–231.
19. **Rousseeuw PJ.** Silhouettes: A graphical aid to the interpretation and validation of cluster analysis. *J Comput Appl Math* 20: 53–65, 1987. doi:10.1016/0377-0427(87)90125-7.
20. **Tan P-N**, **Steinbach M**, **Karpatne A**, **Kumar V.** Introduction to data mining. In: *What's New in Computer Science* (2nd ed.). New York, NY: Pearson, 2018.
21. **Strehl A**, **Ghosh J.** Cluster ensembles: a knowledge reuse framework for combining multiple partitions. *J Mach Learn Res* 3: 583–617, 2002.
22. **Cohen MX.** A tutorial on generalized eigendecomposition for source separation in multichannel electrophysiology (Preprint). arXiv 2104.12356v2, 2021. doi:10.48550/arXiv.2104.12356.
23. **Parra LC**, **Spence CD**, **Gerson AD**, **Sajda P.** Recipes for the linear analysis of EEG. *NeuroImage* 28: 326–341, 2005. doi:10.1016/j.neuroimage.2005.05.032.
24. **van den Heuvel MP**, **Sporns O.** Rich-club organization of the human connectome. *J Neurosci* 31: 15775–15786, 2011. doi:10.1523/JNEUROSCI.3539-11.2011.
25. **Rubinov M**, **Sporns O.** Complex network measures of brain connectivity: uses and interpretations. *NeuroImage* 52: 1059–1069, 2010. doi:10.1016/j.neuroimage.2009.10.003.
26. **Beeler JA**, **Dreyer JK.** Synchronicity: the role of midbrain dopamine in whole-brain coordination. *eNeuro* 6: ENEURO.0345-18.2019, 2019. doi:10.1523/ENEURO.0345-18.2019.
27. **Benchenane K**, **Peyrache A**, **Khamassi M**, **Tierney PL**, **Gioanni Y**, **Battaglia FP**, **Wiener SI.** Coherent theta oscillations and reorganization of spike timing in the hippocampal- prefrontal network upon learning. *Neuron* 66: 921–936, 2010. doi:10.1016/j.neuron.2010.05.013.
28. **Paxinos G**, **Watson C.** *The Rat Brain in Stereotaxic Coordinates: Hard Cover Edition* (6th ed.). Cambridge, MA: Academic Press, 2006.
29. **Schmahmann J**, **Pandya D.** *Fiber Pathways of the Brain*. New York, NY: Oxford University Press, 2006. doi:10.1093/acprof:oso/9780195104233.001.0001.
30. **Gabbott PLA**, **Warner TA**, **Jays PRL**, **Salway P**, **Busby SJ.** Prefrontal cortex in the rat: projections to subcortical autonomic, motor, and limbic centers. *J Comp Neurol* 492: 145–177, 2005. doi:10.1002/cne.20738.
31. **Geisler S**, **Zahm DS.** Afferents of the ventral tegmental area in the rat-anatomical substratum for integrative functions. *J Comp Neurol* 490: 270–294, 2005. doi:10.1002/cne.20668.
32. **Hoover WB**, **Vertes RP.** Anatomical analysis of afferent projections to the medial prefrontal cortex in the rat. *Brain Struct Funct* 212: 149–179, 2007. doi:10.1007/s00429-007-0150-4.
33. **Prensa L**, **Parent A.** The nigrostriatal pathway in the rat: a single-axon study of the relationship between dorsal and ventral tier nigral neurons and the striosome/matrix striatal compartments. *J Neurosci* 21: 7247–7260, 2001. doi:10.1523/JNEUROSCI.21-18-07247.2001.
34. **Gunaydin LA**, **Grosenick L**, **Finkelstein JC**, **Kauvar IV**, **Fenno LE**, **Adhikari A**, **Lammel S**, **Mirzabekov JJ**, **Airan RD**, **Zalocusky KA**, **Tye KM**, **Anikeeva P**, **Malenka RC**, **Deisseroth K.** Natural neural projection dynamics underlying social behavior. *Cell* 157: 1535–1551, 2014. doi:10.1016/j.cell.2014.05.017.
35. **Chang L**, **Tsao DY.** The code for facial identity in the primate brain. *Cell* 169: 1013–1028.e14, 2017. doi:10.1016/j.cell.2017.05.011.
36. **Grimaldi P**, **Kadharbatcha SS**, **Tsao D.** Anatomical connections of the functionally defined "face patches" in the macaque monkey. *Neuron* 90: 1325–1342, 2016. doi:10.1016/j.neuron.2016.05.009.
37. **Moeller S**, **Crapse T**, **Chang L**, **Tsao DY.** The effect of face patch microstimulation on perception of faces and objects. *Nat Neurosci* 20: 743–752, 2017. doi:10.1038/nn.4527.
38. **Krebs RM**, **Heipertz D**, **Schuetze H**, **Duzel E.** Novelty increases the mesolimbic functional connectivity of the substantia nigra/ventral tegmental area (SN/VTA) during reward anticipation: Evidence from high-resolution fMRI. *NeuroImage* 58: 647–655, 2011. doi:10.1016/j.neuroimage.2011.06.038.
39. **Çukur T**, **Nishimoto S**, **Huth AG**, **Gallant JL.** Attention during natural vision warps semantic representation across the human brain. *Nat Neurosci* 16: 763–770, 2013. doi:10.1038/nn.3381.
40. **Raichle ME.** The brain's default mode network. *Annu Rev Neurosci* 38: 433–447, 2015. doi:10.1146/annurev-neuro-071013-014030.
41. **Horvitz JC**, **Stewart T**, **Jacobs BL.** Burst activity of ventral tegmental dopamine neurons is elicited by sensory stimuli in the awake cat. *Brain Res* 759: 251–258, 1997. doi:10.1016/s0006-8993(97)00265-5.
42. **Ljungberg T**, **Apicella P**, **Schultz W.** Responses of monkey dopamine neurons during learning of behavioral reactions. *J Neurophysiol* 67: 145–163, 1992. doi:10.1152/jn.1992.67.1.145.
43. **O'Carroll CM**, **Martin SJ**, **Sandin J**, **Frenguelli B**, **Morris RGM.** Dopaminergic modulation of the persistence of one-trial hippocampus-dependent memory. *Learn Mem* 13: 760–769, 2006. doi:10.1101/lm.321006.

44. **Kamiński J**, **Mamelak AN**, **Birch K**, **Mosher CP**, **Tagliati M**, **Rutishauser U.** Novelty-sensitive dopaminergic neurons in the human substantia nigra predict success of declartive memory formation. *Curr Biol* 28: 1333–1343, 2018. doi:10.1016/j.cub.2018.03.024.
45. **Otmakhova N**, **Duzel E**, **Deutch AY**, **Lisman J.** The hippocampal-VTA loop: the role of novelty and motivation in controlling the entry of information into long-term memory. In: *Intrinsically Motivated Learning in Natural and Artificial Systems*, edited by Baldassarre G, Mirolli M. Berlin, Heidelberg: Springer Berlin Heidelberg, 2013, p. 235–254. doi:10.1007/978-3-642-32375-1.
46. **Kafkas A**, **Montaldi D.** How do memory systems detect and respond to novelty? *Neurosci Lett* 680: 60–68, 2018. doi:10.1016/j.neulet.2018.01.053.
47. **Rajasethupathy P**, **Sankaran S**, **Marshel JH**, **Kim CK**, **Ferenczi E**, **Lee SY**, **Berndt A**, **Ramakrishnan C**, **Jaffe A**, **Lo M**, **Liston C**, **Deisseroth K.** Projections from neocortex mediate top-down control of memory retrieval. *Nature* 526: 653–659, 2015. doi:10.1038/nature15389.
48. **Fujisawa S**, **Buzsaki G.** A 4 Hz oscillation adaptively synchronizes prefrontal, VTA, and hippocampal activities. *Neuron* 72: 153–165, 2011. doi:10.1016/j.neuron.2011.08.018.
49. **Freedberg M**, **Toader AC**, **Wassermann EM**, **Voss JL.** Competitive and cooperative interactions between medial temporal and striatal learning systems. *Neuropsychologia* 136: 107257, 2020. doi:10.1016/j.neuropsychologia.2019.107257.
50. **Jo YS**, **Lee J**, **Mizumori SJY.** Effects of prefrontal cortical inactivation on neural activity in the ventral tegmental area. *J Neurosci* 33: 8159–8171, 2013. doi:10.1523/JNEUROSCI.0118-13.2013.
51. **Dede AJO**, **Smith CN.** The functional and structural neuroanatomy of systems consolidation for autobiographical and semantic memory. *Curr Top Behav Neurosci* 37: 119–150, 2018. doi:10.1007/7854_2016_452.